JOURNAL OF MATERIALS SCIENCE 26 (1991) 2868–2878

Solidification of tin droplets embedded in an aluminium matrix

W. T. KIM, B. CANTOR
Oxford Centre for Advanced Materials and Composites, Department of Materials, Oxford University, Parks Road, Oxford OX1 3PH, UK

The solidification behaviour of tin droplets embedded in an aluminium matrix in a rapidly solidified Al–5 wt% Sn alloy has been investigated by a combination of transmission electron microscopy and differential scanning calorimetry. Detailed transmission electron microscopy shows that rapidly solidified Al–5 wt% Sn consists of about 5 μm diameter columnar aluminium grains, with a fine-scale distribution of 20–300 nm sized tin particles embedded within the aluminium grains, and 100–400 nm sized tin particles at the aluminium grain boundaries. The tin particles exhibit two different orientation relationships with the aluminium matrix and a variety of different faceted shapes: $\{1\,1\,1\}_{Al}\|\{1\,0\,0\}_{Sn}$ and $\langle\bar{2}\,1\,1\rangle_{Al}\|\langle 0\,1\,0\rangle_{Sn}$, with the main facet parallel to $\{1\,1\,1\}_{Al}$ and $\{1\,0\,0\}_{Sn}$; and $\{1\,0\,0\}_{Al}\|\{1\,0\,0\}_{Sn}$ and $\langle 0\,1\,1\rangle_{Al}\|\langle 0\,1\,1\rangle_{Sn}$, with the main facet parallel to $\{1\,0\,0\}_{Al}$ and $\{1\,0\,0\}_{Sn}$. *In situ* heating in the transmission electron microscope shows that the different tin particle shapes are not affected by heat treatment in the solid state, but change into a truncated octahedral shape bounded by $\{1\,1\,1\}_{Al}$ and $\{1\,0\,0\}_{Al}$ facets when the tin particles melt. The $\{1\,0\,0\}_{Al}$–liquid Sn interfacial energy is about 9% larger than the $\{1\,1\,1\}_{Al}$–liquid Sn interfacial energy just above the tin particle melting point, and the $\{1\,0\,0\}_{Al}/\{1\,1\,1\}_{Al}$ interfacial energy anisotropy decreases gradually as the temperature increases above the melting point. Differential scanning calorimeter experiments show that the liquid tin droplets solidify in three stages. Firstly, the larger tin droplets at the aluminium grain boundaries solidify by nucleation on catalytic trace impurities, over a temperature range of 170–140 °C. Secondly and thirdly, the smaller tin particles embedded within the aluminium grains solidify by catalytic nucleation on the $\{1\,0\,0\}_{Al}$ and $\{1\,1\,1\}_{Al}$ facets, over the two temperature ranges of 140–128 °C and 128–115 °C. Catalytic nucleation of the solidification of tin takes place at special sites such as steps or dislocations on the $\{1\,0\,0\}_{Al}$ and $\{1\,1\,1\}_{Al}$ facets with contact angles of 55° and 59°.

1. Introduction

The nucleation pattern during solidification processing determines many important microstructural features, such as the grain size, grain shape, phase structure and alloy segregation, all of which have a significant influence on the mechanical properties of the resulting material products. It is very important therefore to understand in detail the kinetics of nucleation, in order to control the resulting solidification microstructure and properties. Unfortunately, it is inherently difficult to observe the nucleation of solidification, because it involves the formation of very small clusters of solid atoms embedded in a dense liquid matrix [1].

Solidification can take place by either homogeneous or heterogeneous nucleation. In homogeneous nucleation, solid nuclei form in an undercooled liquid by thermal or compositional fluctuations, without any assistance from a nucleation catalyst. In heterogeneous nucleation, solid nuclei again form in an undercooled liquid by thermal or compositional fluctuations, but in this case directly in contact with a nucleation catalyst. Because of the difficulty of removing unknown impurities which can act as nucleation catalysts, most solidification processes take place by heterogeneous nucleation.

To study heterogeneous nucleation, the main problem is to remove unknown impurities. When this has been achieved the effect of a nucleation catalyst can then be assessed by monitoring the undercooling in the liquid at the onset of solidification, i.e. the kinetic barrier to nucleation. The probability of an unknown impurity particle being present in a given mass of liquid is proportional to the volume of the liquid. The most common method of undercooling liquids is therefore to make small droplets to reduce the effect of unknown impurities. Organic emulsifying agents have been used to divide a liquid mass into a large number of small liquid droplets [2–10], and individual droplets have been studied, either on carefully prepared substrates [11–14], without substrates in flight tubes [15–17], by levitation [18–20], or after fluxing to scavenge impurities [21–23]. In most of these experimental studies, calorimetry, dilatometry or microscopy has been used to detect the liquid undercooling at the onset of nucleation. Unfortunately, the reported

0022–2461/91 $03.00 + .12

measurements of liquid undercooling are far from reproducible [24].

An experimental technique which gives more reproducible measurements of liquid undercooling was first devised by Wang and Smith [25] and subsequently used by a variety of other investigators [26–31]. In this technique, thermomechanical treatment is used to manufacture a material consisting of low melting point droplets embedded in a high melting point matrix. The solidification kinetics of the droplets are then monitored by thermal analysis methods during cooling below their melting point. The main advantage of this technique is that the nucleation of solidification takes place in clean liquid droplets in contact with a solid matrix, with a known microstructure, composition and shape.

The present paper describes an investigation into the solidification of tin droplets embedded in an aluminium matrix in a rapidly solidified Al–5 wt % Sn alloy, using a combination of differential scanning calorimetry (DSC) to monitor the tin droplet solidification kinetics, and transmission electron microscopy (TEM) to examine the solidified tin particle microstructure and morphology. The simple eutectic Al–Sn alloy system [32] was chosen to reduce compositional and microstructural changes in both the particles and matrix during heat treatment. This can be seen on the Al–Sn equilibrium phase diagram because (a) the eutectic composition is close to pure tin, (b) the solubility of tin in solid aluminium is extremely low, and (c) the aluminium liquidus line is steep in the Sn-rich liquid region.

2. Experiments

A chill-cast ingot of composition Al–5 wt % Sn was manufactured by induction melting 99.999% pure aluminium and tin in a recrystallized alumina crucible under a dynamic Ar atmosphere. Specimens of the Al–5 wt % Sn alloy ingot were then rapidly solidified by melt spinning. Alloy charges of approximately 3 g were remelted in quartz crucibles under a dynamic Ar atmosphere, held for approximately 100 s at 800 °C and then ejected with an Ar overpressure of 14 kPa through a slit nozzle, on to the outer surface of a Cu drum rotating with a surface velocity of 16 m s^{-1}. The resulting melt spun ribbons were typically 1 cm wide, 70 μm thick and several metres long. Ribbon compositions were analysed on polished cross-sections in a Cameca CAMEBAX wavelength X-ray microanalyser operating at an accelerating voltage of 20 kV, and were determined to be Al–5.05 wt % Sn.

The tin solidification behaviour in the Al–5 wt % Sn melt spun ribbons were monitored by heating and cooling experiments in a Dupont 1090 thermal analyser fitted with a 910 DSC module. Individual 15–25 mg Al–5 wt % Sn ribbon samples were sealed in aluminium cans, heated from 100–260 °C at a rate of 5 °C min^{-1}, held for 600 s, and then re-cooled to 100 °C at a cooling rate in the range 0.5–12 °C min^{-1}, all under a dynamic Ar atmosphere. During each heating and cooling experiment, differences in heat flow to and from the Al–5 wt % Sn ribbon sample and a similarly heat treated reference sample were continuously recorded at maximum sensitivity on a microcomputer for subsequent detailed examination.

For TEM observations, thin foil specimens were prepared from the as-melt spun and heat-treated ribbons by mechanical polishing with SiC paper, followed by twin jet electropolishing in a 75 vol % methanol + 25 vol % nitric acid solution at a temperature between −30 and −50 °C. The microstructures of the resulting thin foils were examined in Jeol 100C and Phillips CM12 TEMs operating at 100 and 120 kV, respectively.

3. Results

3.1. Microstructure

Fig. 1a and b show typical bright-field TEM micrographs of the as-melt spun Al–5 wt % Sn alloy, from the chilled surface in contact with the rotating Cu drum and from the unchilled surface in contact with the atmosphere respectively. The as-melt spun Al–5 wt % Sn microstructure consisted of a fine-scale distribution of bct β-Sn particles embedded in a matrix of approximately 5 μm diameter fcc α-Al grains. About 65 vol % tin particles were distributed within the matrix aluminium grains, and the remaining 35 vol % were distributed the aluminium grain boundaries. Fig. 2 shows the size distribution of the tin particles embedded within the aluminium grains. The diameters of the tin particles within the aluminium grains ranged from 20–300 nm, with an average particle diameter of 90 nm, and increased progressively as the solidification rate decreased from the chilled to the unchilled melt spun ribbon surface. The diameters of the tin particles at the aluminium grain boundaries

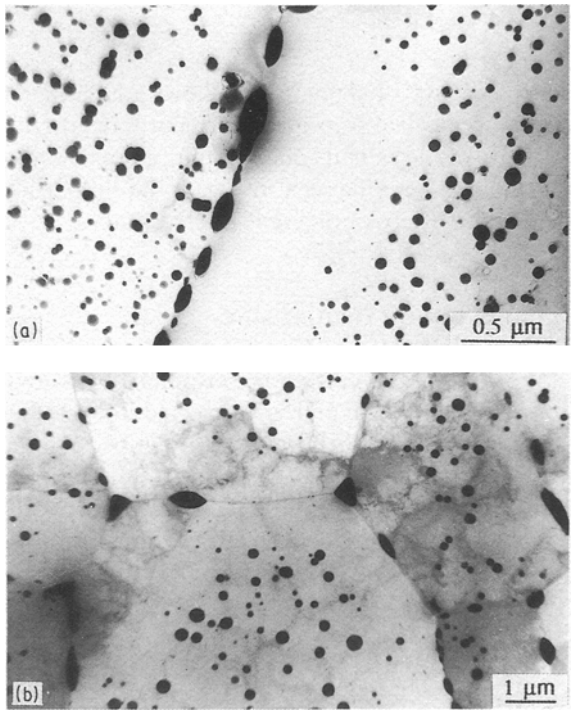

Figure 1 Typical bright-field transmission electron micrographs of as-melt spun Al–5 wt % Sn, showing a fine-scale distribution of tin particles embedded in a matrix of aluminium: (a) near the chilled surface; and (b) near the unchilled surface.

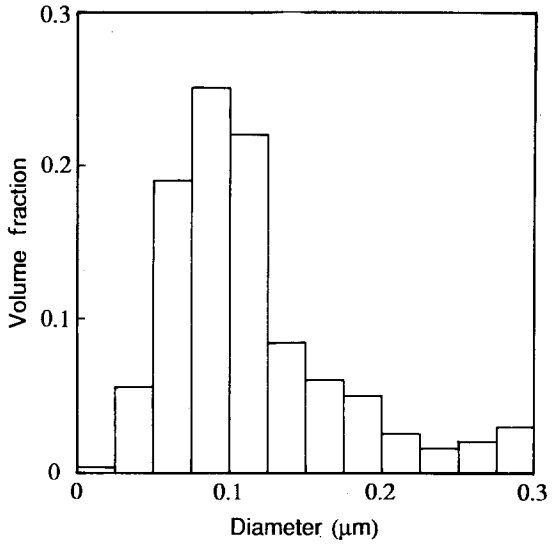

Figure 2 Histogram showing the size distribution of tin particles embedded within the matrix aluminium grains.

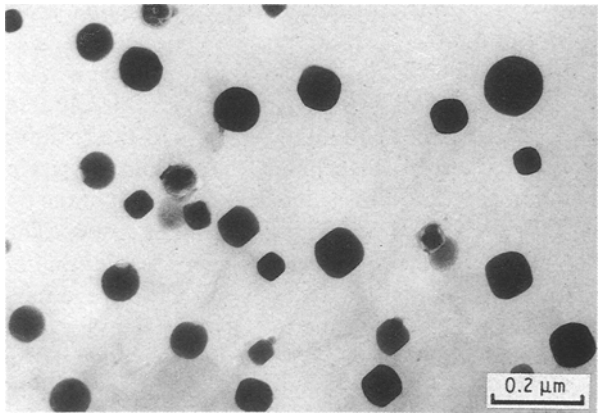

Figure 3 Typical bright-field transmission electron micrograph of tin particles embedded within an aluminium grain, showing a variety of different faceted shapes.

ranged from 100–400 nm. Fig. 3 shows a high-magnification bright-field transmission electron micrograph of the tin particles embedded within a single aluminium grain. As can be seen in Fig. 3, the tin particles exhibited a variety of different faceted shapes.

3.2. Orientation relationship

The orientation relationships between the tin particles and the aluminium matrix were examined by analysis of superimposed β-Sn and α-Al selected-area electron diffraction patterns (SADPs) from a number of different tin particles. Fig. 4a–h show a series of four examples of superimposed tin and aluminium SADPs from different tin particles, together with corresponding schematic analyses. The orientation relationships between the tin particles and the aluminium matrix were divided into two different groups. About half of the embedded tin particles exhibited an orientation relationship within about $\pm 10°$ from $\{1\,1\,1\}_{Al} \| \{1\,0\,0\}_{Sn}$ and $\langle \bar{2}\,1\,1 \rangle_{Al} \| \langle 0\,1\,0 \rangle_{Sn}$ as shown in Fig. 4a–d. The other half of the embedded tin particles exhibited an orientation relationship within $\pm 10°$ from $\{1\,0\,0\}_{Al} \| \{1\,0\,0\}_{Sn}$ and $\langle 0\,1\,1 \rangle_{Al} \| \langle 0\,1\,1 \rangle_{Sn}$ as shown in Fig. 4e–h. Fig. 5 shows the full set of orientation relationships obtained from a total of 22 superimposed tin and aluminium SADPs, in the form of $(1\,0\,0)_{Sn}$–$(0\,1\,0)_{Sn}$–$(0\,0\,1)_{Sn}$ triangles superimposed on a standard $(0\,0\,1)_{Al}$ stereographic projection.

The shapes of the tin particles were quite varied, as expected from the spread of orientation relationships shown in Figs 4 and 5. Figs 6 and 7 show two examples of tin particle shapes. Fig. 6a shows a bright-field transmission electron micrograph of a faceted tin particle, Fig. 6b shows a corresponding superimposed tin and aluminium SADP, and Fig. 6c shows a schematic analysis of the SADP. For this tin particle, the main facet was parallel to $(1\,1\,1)_{Al}$ and $(1\,0\,0)_{Sn}$, with less sharply defined facets parallel to $(1\,\bar{1}\,\bar{1})_{Al}$ and $(1\,0\,0)_{Al}$. Fig. 7a shows a bright-field transmission electron micrograph of another faceted tin particle, Fig. 7b shows a corresponding superimposed tin and aluminium SADP, and Fig. 7c shows a schematic analysis of the SADP. For this tin particle, the main facet was parallel to $(1\,0\,0)_{Al}$ and $(1\,0\,0)_{Sn}$ with additional facets parallel to $(1\,1\,\bar{1})_{Al}$ and $(1\,\bar{1}\,1)_{Al}$. For those tin particles which exhibited an orientation relationship with $(1\,1\,1)_{Al} \| (1\,0\,0)_{Sn}$, the main facet plane was always parallel to $(1\,1\,1)_{Al}$ and $(1\,0\,0)_{Sn}$ as shown in Fig. 6; and for those tin particles which exhibited an orientation relationship with $(1\,0\,0)_{Al} \| (1\,0\,0)_{Sn}$, the main facet plane was always parallel to $(1\,0\,0)_{Al}$ and $(1\,0\,0)_{Sn}$ as shown in Fig. 7. Dislocations were sometimes present at the tin particle/aluminium matrix interface, as shown in Fig. 6a, and shrinkage voids were sometimes present at the corners of the tin particle facets, as shown in the upper right corner of the particle in Fig. 7a.

3.3. *In situ* heating

The variation of tin particle shape as a function of temperature was investigated by *in situ* heating experiments in the TEM. Fig. 8a–c show a series of bright-field transmission electron micrographs of the cross-sectional shapes of three tin particles, at room temperature, 200 and 250 °C, respectively. The particles were all oriented normal to the $[1\,1\,0]_{Al}$ direction, as shown in the SADP and corresponding schematic analysis of Fig. 8d and e, and exhibited different orientation relationships with the aluminium matrix, and different cross-sectional shapes at room temperature. During heating in the solid state, there was almost no change in the shape of any of the three tin particles, as shown in Fig. 8b. At a temperature of 250 °C, however, above the tin particle melting point (i.e. the Al–Sn eutectic temperature of 228 °C [32]) all three liquid tin droplets exhibited the same distorted hexagonal cross-sectional shape as shown in Fig. 8c. This cross-sectional shape is characteristic of a truncated octahedral particle shape bounded by $\{1\,1\,1\}_{Al}$ and $\{1\,0\,0\}_{Al}$ facets [24].

Fig. 9a–e show another series of bright-field transmission electron micrographs of a tin particle cross-sectional shape, at several temperatures between 200 and 300 °C, again oriented normal to the $[1\,1\,0]_{Al}$ direction. As with the three particles in Fig. 8a–c, there

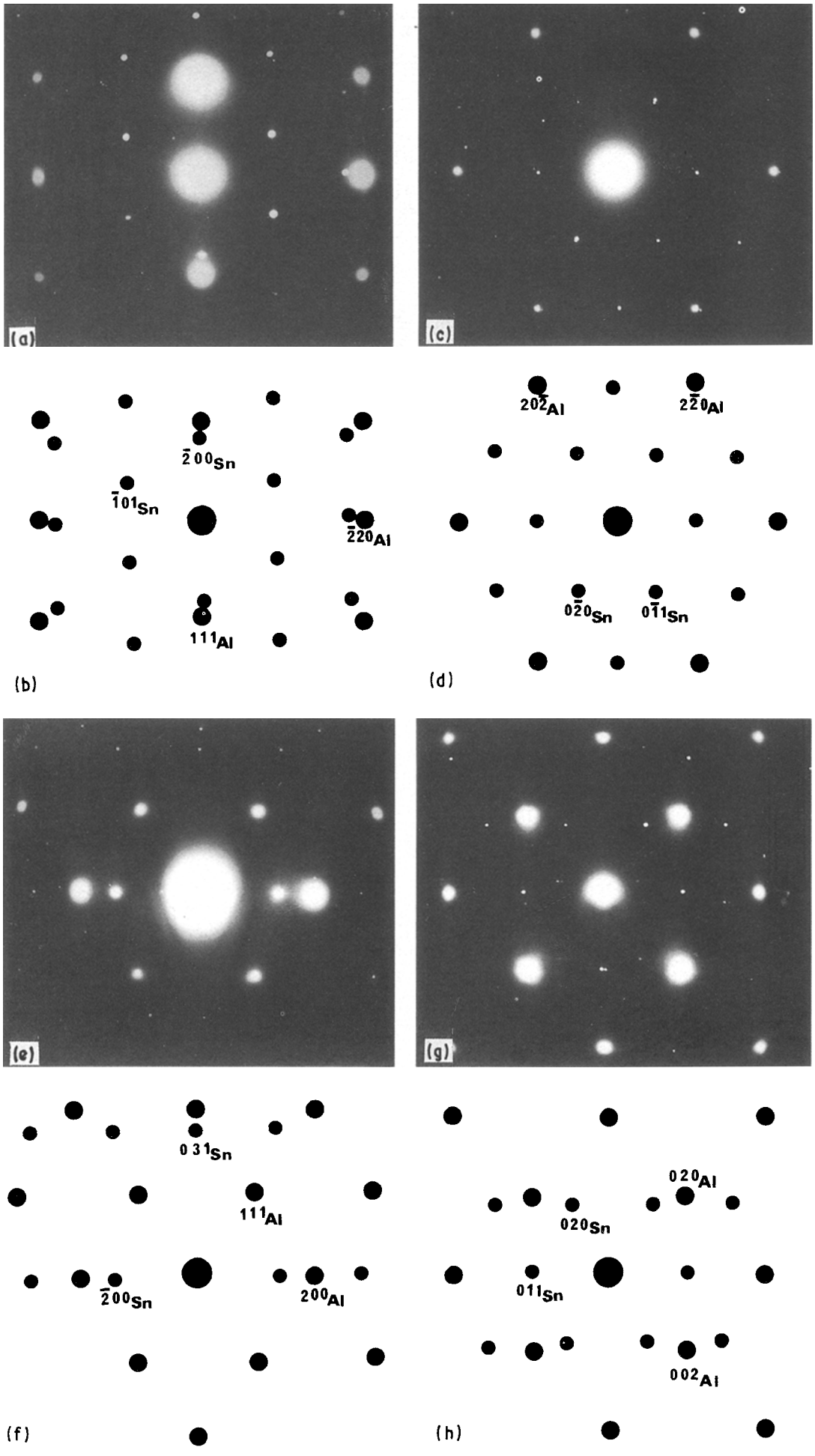

Figure 4 Superimposed bct β-Sn and fcc α-Al SADP from four different tin particles, together with corresponding schematic analyses: (a) and (b) superimposed $[1\,1\,\bar{2}]_{Al}$ and $[0\,1\,0]_{Sn}$ zones; (c) and (d) superimposed $[1\,1\,1]_{Al}$ and $[1\,0\,0]_{Sn}$ zones; (e) and (f) superimposed $[0\,1\,\bar{1}]_{Al}$ and $[0\,1\,\bar{3}]_{Sn}$; and (g) and (h) superimposed $[1\,0\,0]_{Al}$ and $[1\,0\,0]_{Sn}$.

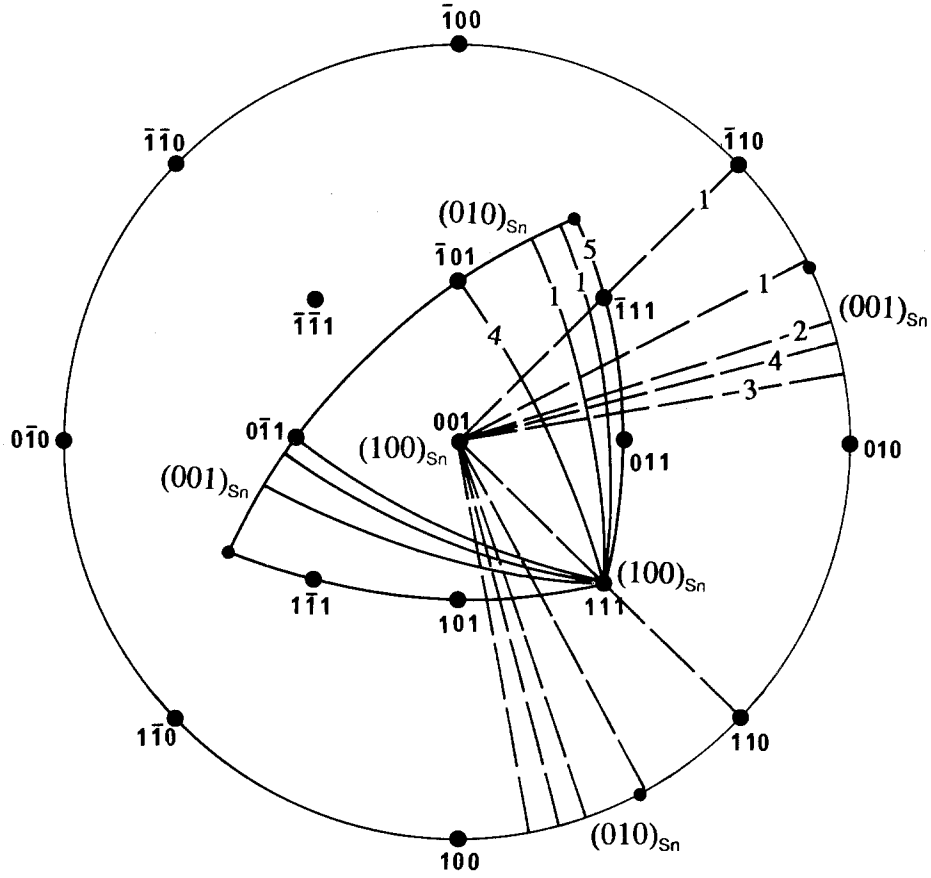

Figure 5 Orientation relationships between tin particles and the surrounding aluminium matrix, plotted as $(1\,0\,0)_{Sn}$–$(0\,1\,0)_{Sn}$–$(0\,0\,1)_{Sn}$ triangles superimposed on a standard $(0\,0\,1)_{Al}$ stereographic projection. The figure on each $(1\,0\,0)_{Sn}$–$(0\,1\,0)_{Sn}$–$(0\,0\,1)_{Sn}$ triangle indicates the number of times this orientation relationship was observed.

was no change in the tin particle shape during heating in the solid state. Just above the tin particle melting point of 228 °C, however, the liquid tin droplet again exhibited a distorted hexagonal cross-sectional shape, characteristic of a truncated octahedral particle shape bounded by $\{1\,1\,1\}_{Al}$ and $\{1\,0\,0\}_{Al}$ facets, as shown in Fig. 9b. As the temperature increased further above the tin particle melting point, the $\{1\,0\,0\}_{Al}$ facet disappeared as shown in Fig. 9c, but the $\{1\,1\,1\}_{Al}$ facets persisted to higher temperatures as shown in Fig. 9c–e. The aluminium grain boundaries and the tin droplets began to migrate at higher temperatures, making *in situ* heating experiments difficult above 300 °C.

From the Gibbs Wulff theorem [33], the surface energy of each pair of facets is proportional to the facet separation. Fig. 10 shows the ratio of $\{1\,0\,0\}_{Al}/\{1\,1\,1\}_{Al}$ interfacial energies above the tin particle melting point, measured from the facet separations of tin droplet shapes such as Fig. 9b–e. The $\{1\,0\,0\}_{Al}$ interfacial energy was about 9% larger than $\{1\,1\,1\}_{Al}$ interfacial energy just above the tin particle melting point, and the $\{1\,0\,0\}_{Al}/\{1\,1\,1\}_{Al}$ interfacial energy anisotropy decreased gradually as the temperature increased above the melting point.

3.4. Sn particle solidification

Fig. 11 shows a typical DSC trace obtained from the as-melt spun Al–5 wt % Sn alloy during cooling at 2.5 °C min^{-1} from 260–100 °C. Solidification of the tin droplets took place with three exothermic peaks in the DSC traces. As the temperature decreased, the first broad exothermic peak appeared over a temperature range of approximately 170–140 °C, followed by two sharper exothermic peaks over temperature ranges of approximately 140–128 °C and 128–115 °C, respectively. The three exothermic peaks overlapped to some extent, preventing accurate determination of the onset temperatures, as shown in Fig. 11. At each cooling rate in the DSC, however, the peak temperatures of the sharper second and third exothermic peaks were reproducible to within ±0.5 °C. Fig. 12 shows the resulting variations of the peak temperatures as a function of the cooling rate. As the imposed cooling rate increased from 0.5–12 °C min^{-1}, the peak temperatures of the second and third exothermic peaks decreased from 136–131 °C, and from 126–121 °C, respectively.

The solidification of the tin droplets in the three exothermic peaks was further investigated by a series of reheating experiments. DSC specimens were heated to 260 °C to melt all the tin particles, then cooled to a temperature in the range 100–200 °C to solidify some of the tin droplets, and finally reheated again to 260 °C to melt those tin particles which solidified during the cooling cycle. Exothermic and endothermic peak shapes and temperatures were not affected by reheating and cooling, indicating considerable resistance to tin particle coarsening during heat treatment. Fig. 13 shows an example of the resulting endothermic and exothermic peaks, monitored in the DSC during heat-

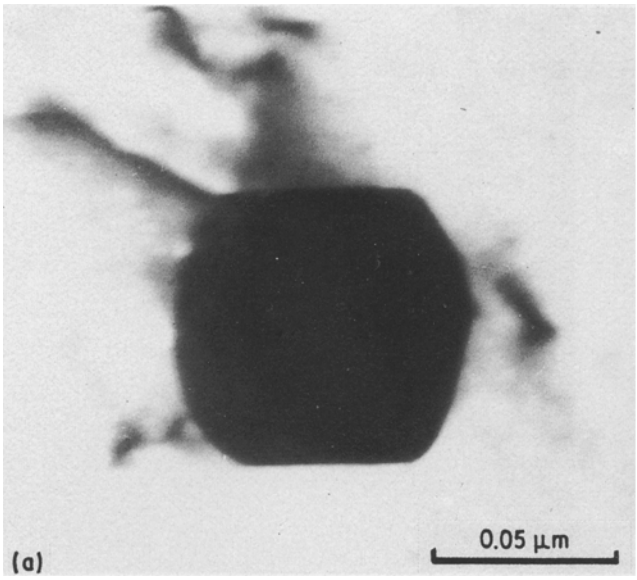

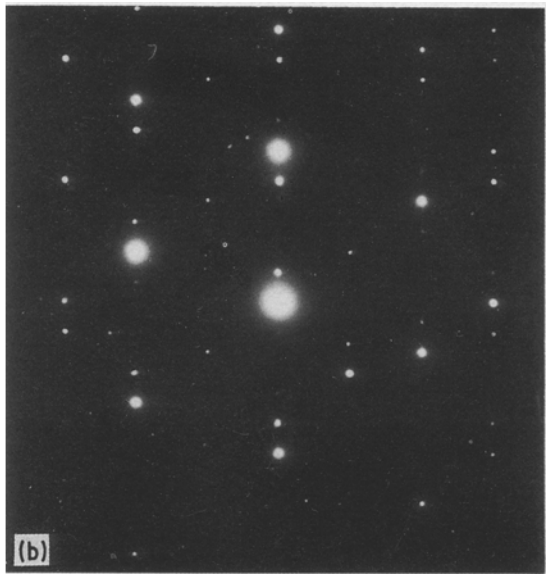

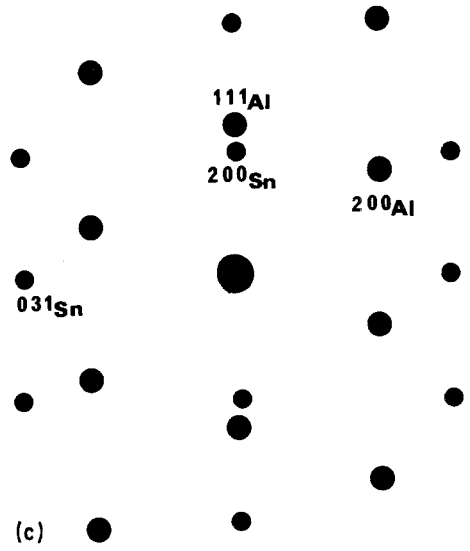

Figure 6 (a) Bright-field transmission electron micrograph of a faceted tin particle; (b) corresponding SADP showing superimposed $[0\,1\,\bar{3}]_{Sn}$ and $[0\,1\,\bar{1}]_{Al}$ zones; and (c) schematic analysis of the SADP.

ing and cooling. The endothermic peak area during heating from 100–260 °C was 2.95 J g^{-1}, corresponding to complete melting of all the embedded tin particles in the Al–5 wt % Sn alloy. However, the endothermic peak area during reheating from 140–260 °C was 1.0 J g^{-1}, corresponding to about 35% of the embedded tin particles. In other words, 35% tin particles solidified in the first broad exothermic peak during the previous cooling cycle, and the other 65% solidified in the sharper second and third exothermic peaks.

4. Discussion

4.1. Melt spun microstructure

The microstructure of rapidly solidified Al–5 wt % Sn consists of a fine-scale distribution of faceted β-Sn particles embedded in an α-Al matrix, as shown in Figs 1 and 3. Approximately 65 vol % tin particles are distributed within the 5 μm sized aluminium grains, with particle diameters ranging from 20–300 nm, and an average particle diameter of 90 nm. The remaining 35 vol % tin particles are distributed at the aluminium grain boundaries, with particle diameters ranging from 100–400 nm. The tin particles exhibit two different types of orientation relationship with the aluminium matrix, about half within $\pm 10°$ from $\{1\,1\,1\}_{Al}\|\{1\,0\,0\}_{Sn}$ and $\langle\bar{2}\,1\,1\rangle_{Al}\|\langle 0\,1\,0\rangle_{Sn}$, and the remaining half within $\pm 10°$ from $\{1\,0\,0\}_{Al}\|\{1\,0\,0\}_{Sn}$ and $\langle 0\,1\,1\rangle_{Al}\|\langle 0\,1\,1\rangle_{Sn}$. The tin particles exhibit a variety of different faceted shapes, with the main facet plane being either $\{1\,1\,1\}_{Al}\|\{1\,0\,0\}_{Sn}$ or $\{1\,0\,0\}_{Al}\|\{1\,0\,0\}_{Sn}$ depending on the orientation relationship with the aluminium matrix.

The Al–Sn alloy system has a simple eutectic phase diagram, with a eutectic point at 228 °C and 99.5 wt % tin, and with very limited solubility of tin in f c c α-Al and aluminium in b c t β-Sn. During melt spinning of the Al–5 wt % Sn alloy, the evolution of the microstructure can be described as follows.

(a) Primary aluminium solidification: when the liquid temperature falls below the liquidus temperature of about 652 °C [32], primary aluminium nucleates on the chilled surface in contact with the Cu drum, and grows laterally over the chilled surface to establish a stable set of columnar grains solidifying through the thickness of the melt spun ribbon.

(b) tin droplet formation: during primary aluminium solidification, tin droplets can form, and become entrained in the aluminium matrix, by two different mechanisms. Firstly, tin atoms can partition at the primary aluminium solid/liquid interface, segregate into intercellular and interdendritic regions, and then be incorporated as droplets by the advancing aluminium interface. Secondly, tin droplets can form by liquid-phase separation in the undercooled liquid ahead of the primary aluminium solid/liquid interface, and then be incorporated by the advancing interface. This mechanism assumes that there is a submerged liquid miscibility gap, as indicated by the nearly horizontal shape of the equilibrium liquidus on the Al–Sn phase diagram.

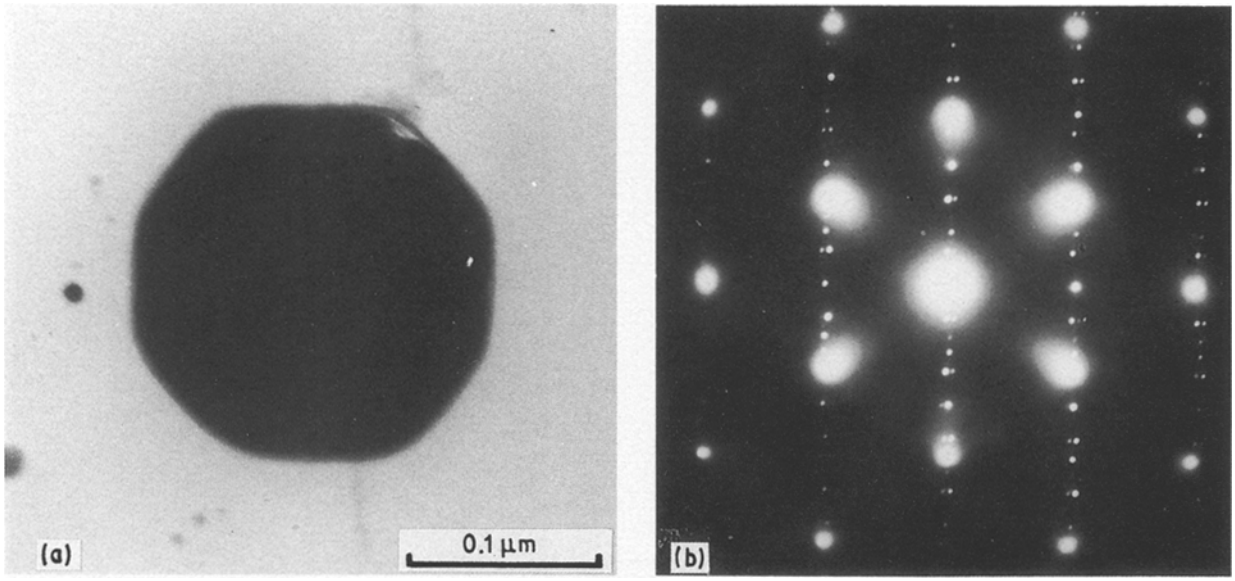

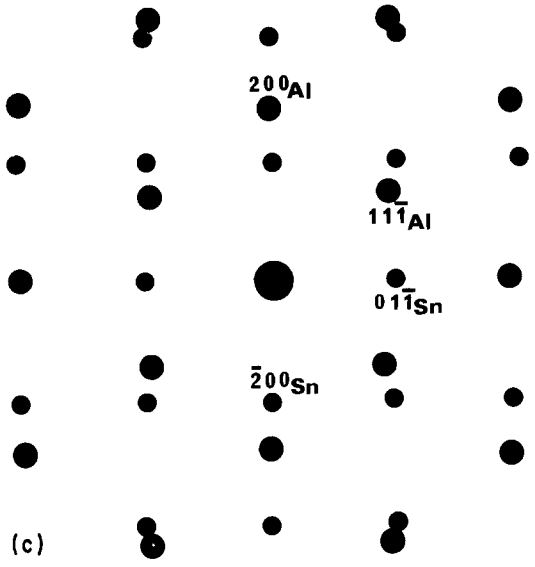

Figure 7 (a) Bright-field transmission electron micrograph of a faceted tin particle; (b) corresponding SADP showing superimposed $[0\,1\,1]_{Sn}$ and $[0\,1\,1]_{Al}$ zones; and (c) schematic analysis of the SADP.

(c) Faceting: as the temperature decreased from the liquidus temperature of 652 °C to the eutectic temperature of 228 °C, the tin droplets modify their shape to reduce their total surface energy. As shown in Figs 8 and 9, the liquid tin droplets gradually develop a truncated octahedral shape, forming $\{1\,1\,1\}_{Al}$ facets below approximately 300 °C, and then $\{1\,0\,0\}_{Al}$ facets close to the eutectic temperature of 228 °C. Just above the eutectic point, the truncated octahedral shape of the liquid tin droplets is similar to the previously reported shape of liquid Pb [29], Cd [30] and In [31] droplets embedded in an aluminium matrix. In other words, the shapes of liquid droplets embedded in aluminium are controlled by the fcc aluminium crystallography.

(d) Droplet solidification: on cooling below the eutectic temperature of 228 °C, the tin droplets solidify by epitaxial heterogeneous nucleation on the surrounding aluminium matrix facets. The catalytic nucleation process leads to two types of orientation relationship between the tin particles and the surrounding aluminium matrix, as shown in Figs 3 and 4. The droplet solidification behaviour is discussed in more detail in the next section.

4.2. Sn droplet solidification

When rapidly solidified Al–5 wt % Sn is heated to 260 °C and then cooled, the liquid tin droplets embedded in the aluminium matrix solidify in three stages, as indicated by the three exothermic peaks on the DSC traces shown in Figs 11 and 12. As the temperature decreases, the first broad exothermic peak appears over a temperature range of approximately 170–140 °C, followed by two sharper exothermic peaks over temperature ranges of approximately 140–128 °C and 128–115 °C, respectively. There are two reasons for associating the broad exothermic peak with the solidification of the larger tin droplets at the aluminium grain boundaries. Firstly, 35% tin particles are at the aluminium grain boundaries as shown in Fig. 1, and 35% tin particles solidify in the first broad exothermic peak as shown in the reheating experiments of Fig. 13. Secondly, the larger tin droplets at the aluminium grain boundaries solidify with relatively little undercooling below the eutectic temperature, because they are more easily contaminated by catalytic trace impurities than the smaller tin droplets embedded within the aluminium grains.

The second and third exothermic peaks correspond to solidification of the small tin droplets embedded in the aluminium grains. These two exothermic peaks have previously been reported to arise from a bimodal distribution of tin droplet sizes [27]. However, the present experiments do not show a bimodal distribution as shown in Fig. 2, although there is considerable variation in tin particle size. The clear separation into two exothermic peaks, as shown in Figs 11 and 13 indicates, therefore, that there are two different types of heterogeneous nucleation site at the droplet/matrix interface. The two exothermic peaks probably correspond to the two different orientation relationships between the tin particles and the aluminium matrix as shown in Figs 4 and 5, and the two main facets of $\{1\,1\,1\}_{Al}\|\{1\,0\,0\}_{Sn}$ or $\{1\,0\,0\}_{Al}\|\{1\,0\,0\}_{Sn}$ as shown in

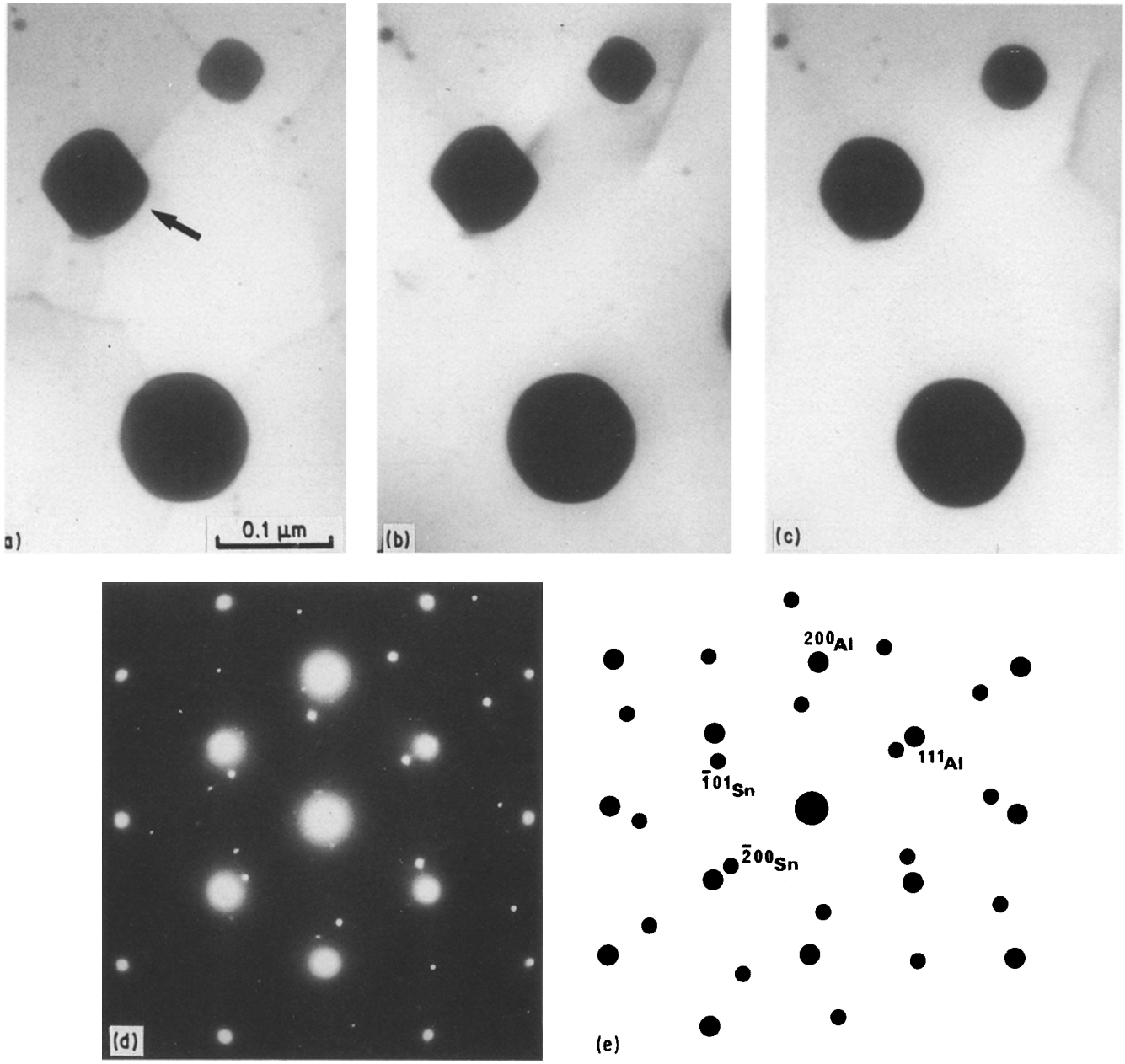

Figure 8 Series of bright-field micrographs during *in situ* heating in the TEM, showing the temperature variations of the cross-sectional shapes of three tin particles oriented normal to $[1\,1\,0]_{Al}$: (a) room temperature; (b) 200 °C; (c) 250 °C; (d) corresponding SADP showing superimposed $[0\,1\,0]_{Sn}$ and $[0\,1\,\bar{1}]_{Al}$ zones from the tin particle marked by an arrow in (a); and (e) schematic analysis of the SADP.

Figs 6 and 7. The tin droplet crystallography seems to indicate that the droplets nucleate epitaxially on either the $\{1\,1\,1\}_{Al}$ or $\{1\,0\,0\}_{Al}$ facets, with $\{1\,0\,0\}_{Sn}$ parallel to the nucleating facet in each case. Unfortunately, there is no available information on the $\{1\,1\,1\}_{Al}\|\{1\,0\,0\}_{Sn}$ and $\{1\,0\,0\}_{Al}\|\{1\,0\,0\}_{Sn}$ surface energies, and it is difficult to tell which exothermic peak corresponds to which nucleating facet. Also it is not clear why different tin particles nucleate on different facets. This may be associated with some other microstructural effect, such as the presence of dislocations at the droplet/matrix interface as shown in Fig. 6a.

4.3. Sn nucleation kinetics

Fig. 14 shows schematically the nucleation of a spherical cap of solid tin on a catalytic $(h\,k\,l)$ facet of the aluminium matrix surrounding a liquid tin particle in melt spun Al–5 wt % Sn. At any temperature, T, below the Al–Sn eutectic temperature, T_e, the heterogeneous nucleation rate, I, within each tin droplet is given by [34, 35]

$$I = A\exp[-B/(T_e - T)^2 T] \quad (1)$$

where $A = N_c(kT/h)\exp(-Q/kT)$, N_c is the number of potential catalytic sites per droplet, k and h are Boltzmann's and Planck's constants, respectively, Q is the activation free energy for transporting a tin atom across the tin solid–liquid interface, $B = K\sigma^3 T_e^2 f(\theta)/kL^2$, K is a shape factor equal to $16\pi/3$ for a spherical cap-shaped nucleus, σ is the tin solid–liquid interfacial energy, $f(\theta) = (2 - 3\cos\theta + \cos^3\theta)/4$, θ is the contact angle at the solid Al–solid Sn–liquid Sn triple point, and L is the latent heat of solidification of tin.

Almost all the tin particles are single crystals, indicating that only one nucleation event takes place in each tin droplet, and that the post-nucleation growth

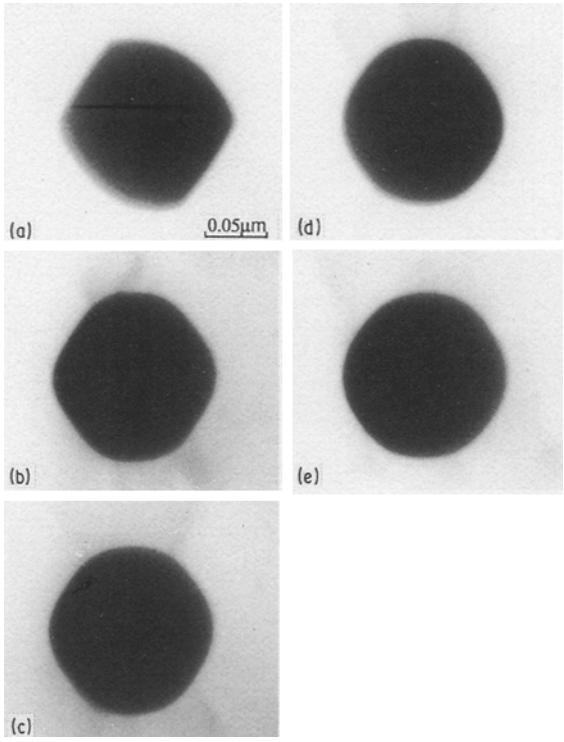

Figure 9 Series of bright-field micrographs during *in situ* heating in the TEM, showing the temperature variation of the cross-sectional shape of a tin particle oriented normal to $[1\,1\,0]_{Al}$: (a) 200 °C; (b) 235 °C; (c) 250 °C; (d) 265 °C; and (e) 300 °C.

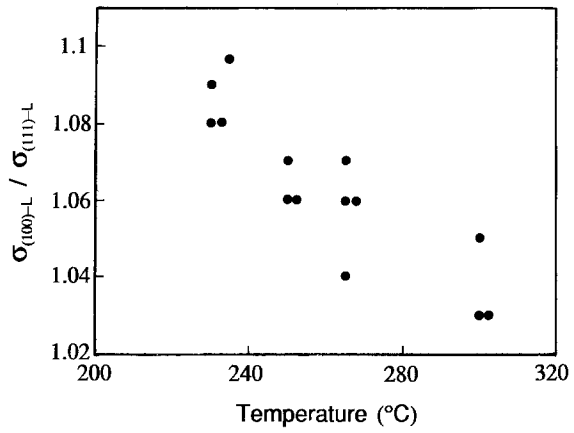

Figure 10 Variation of the ratio of $\{1\,0\,0\}_{Al}$/liquid Sn and $\{1\,1\,1\}_{Al}$/liquid Sn interfacial energies as a function of temperature.

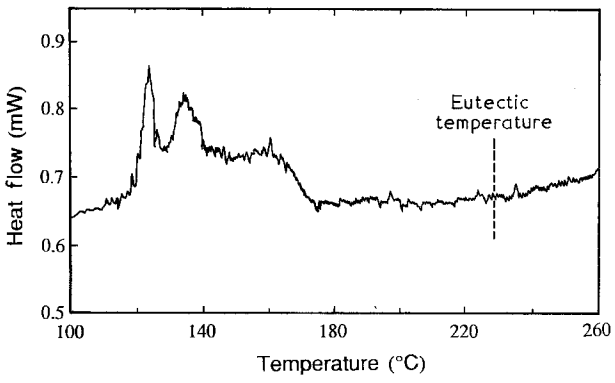

Figure 11 Typical DSC trace obtained from melt spun Al–5 wt % Sn during cooling at 2.5 °C min^{-1} from 260–100 °C.

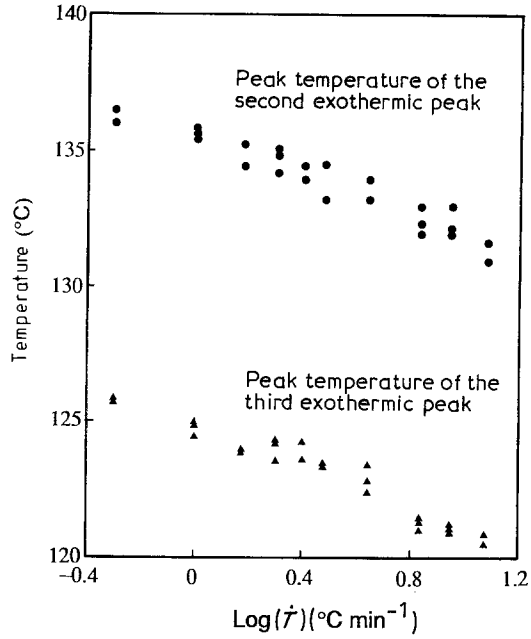

Figure 12 Peak temperatures of the second and third exothermic peaks as a function of the imposed cooling rate in the DSC.

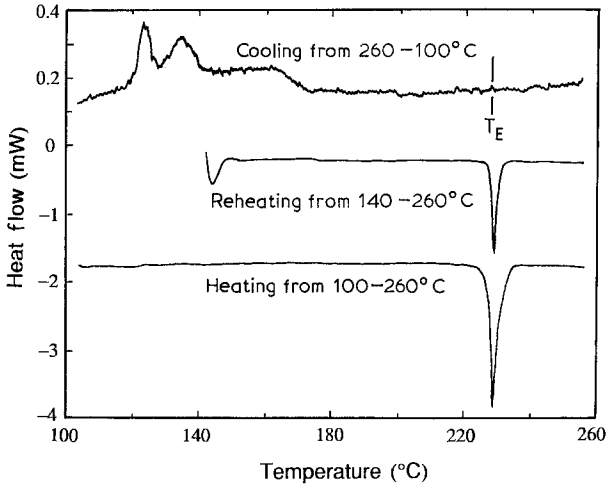

Figure 13 Endothermic and exothermic peaks monitored in the DSC during heating and cooling cycles at 5 and 2.5 °C min^{-1}, respectively.

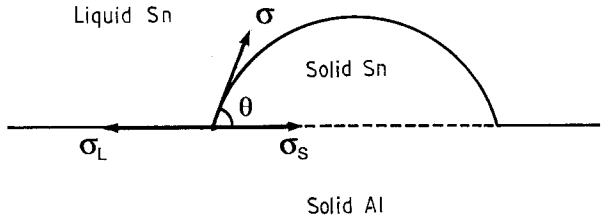

Figure 14 Schematic diagram of a spherical cap-shaped solid tin nucleus on a catalytic $(h\,k\,l)$ facet of the aluminium matrix surrounding a liquid tin droplet.

rate is very fast. The fraction of solid tin particles, Z, is then given by the differential equation [36]

$$dZ/dt = I(1 - Z) \quad (2)$$

With decreasing temperature below T_e, the tin droplet solidification rate, dZ/dt, increases with increasing

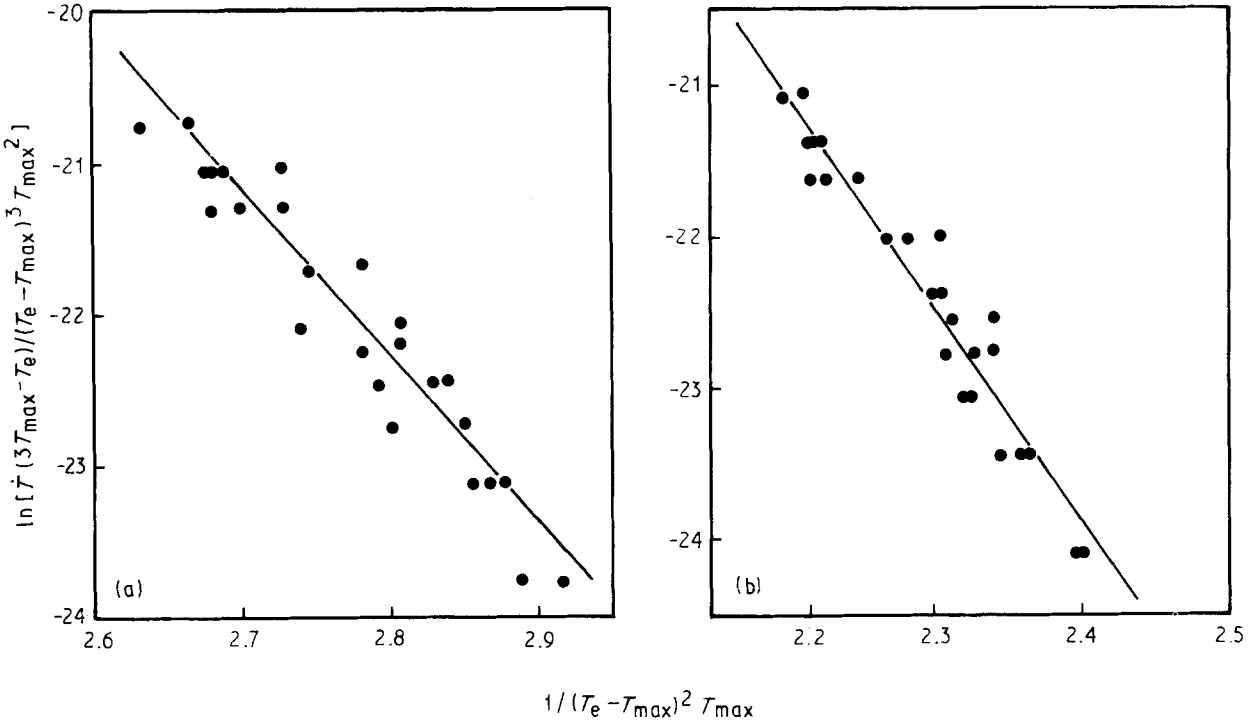

Figure 15 Variation of $\ln[\dot{T}(3T_{max} - T_e)^3/(T_e - T_{max})^2 T_{max}]$ with $1/(T_e - T_{max})^3 T_{max}^2$ from (a) the second, and (b) the third exothermic peak.

nucleation rate, I, reaches a maximum, and then decreases as the solid fraction Z approaches 1.

At a constant cooling rate, $\dot{T}$, the tin particle solidification rate has its maximum value when $d/dT(dZ/dt) = -\dot{T}^{-1}d^2Z/dt^2 = 0$. From Equations 1 and 2, this corresponds to a temperature, T_{max}, given by [36]

$$B\dot{T}(3T_{max} - T_e)/A(T_e - T_{max})^3 T_{max}^2 = \exp[-B/(T_e - T_{max})^2 T_{max}] \quad (3)$$

Equation 3 can be used to calculate the contact angle, θ, and the number of potential catalytic nucleation sites, N_c, from DSC results such as shown in Figs 11 and 12. Fig. 15a and b show the variations of $\ln[\dot{T}(3T_{max} - T_e)^2/(T_e - T_{max})^3 T_{max}^2]$ with $1/(T_e - T_{max})^3 T_{max}^2$ replotted from Fig. 12 for the second and third exothermic peaks, respectively. As expected from Equation 3, Fig. 15a and b show good linear relationships between these two parameters. Least squares best fit values of A and B are $4.3 \times 10^{11}\ s^{-1}$ and $1.09 \times 10^8\ K^3$, respectively, for the second exothermic peak, and $4.9 \times 10^{12}\ s^{-1}$ and $1.4 \times 10^8\ K^3$, respectively, for the third exothermic peak. With $\sigma = 84\ mJ\ m^{-2}$ [37], $L = 4.4 \times 10^8\ J\ m^{-3}$ [38], and $\exp(-Q/kT_e) = 0.01$ [35], the corresponding values of σ and N_c are 55° and 4×10^2, respectively, for the second exothermic peak, and 59° and 5×10^3, respectively, for the third exothermic peak. The number of atoms per droplet at the solid Al–liquid Sn interface is approximately 4×10^5, several orders of magnitude greater than the calculated value of N_c. This indicates that nucleation can only take place at special sites such as steps or dislocations on the $\{1\,0\,0\}_{Al}$ and $\{1\,1\,1\}_{Al}$ facets. The calculated N_c values correspond to 1.6×10^{16} and $1.8 \times 10^{17}\ m^{-2}$ potential catalytic nucleation sites per unit area of solid Al/liquid Sn interface.

5. Conclusions

1. The microstructure of rapidly solidified Al–5 wt % Sn consists of fine-scale faceted β-Sn particles embedded in an aluminium matrix. Approximately 65 vol % tin particles are distributed within the matrix aluminium grains, with particle diameters ranging from 20–300 nm and an average particle diameter of 90 nm. The remaining 35 vol % tin particles are distributed at the aluminium grain boundaries, with particle diameters ranging from 100–400 nm.

2. The tin particles exhibit two different orientation relationships with the aluminium matrix. About half of the tin particles are within ±10° from $\{1\,1\,1\}_{Al}\|\{1\,0\,0\}_{Sn}$ and $\langle\bar{2}\,1\,1\rangle_{Al}\|\langle 0\,1\,0\rangle_{Sn}$, and the remaining half are within ±10° from $\{1\,0\,0\}_{Al}\|\{1\,0\,0\}_{Sn}$ and $\langle 0\,1\,1\rangle_{Al}\|\langle 0\,1\,1\rangle_{Sn}$.

3. The faceted tin particles exhibit a variety of different shapes, with the main facet plane being either $\{1\,1\,1\}_{Al}\|\{1\,0\,0\}_{Sn}$ or $\{1\,0\,0\}_{Al}\|\{1\,0\,0\}_{Sn}$ depending on the orientation relationship.

4. Just above the tin particle melting point, the liquid tin droplets exhibit a truncated octahedral shape bounded by $\{1\,1\,1\}_{Al}$ and $\{1\,0\,0\}_{Al}$ facets, similar to previous observations of liquid Pb, Cd and In droplets embedded in aluminium. The $\{1\,0\,0\}_{Al}$ interfacial energy is about 9% larger than the $\{1\,1\,1\}_{Al}$ interfacial energy just above the tin particle melting point, and the $\{1\,0\,0\}_{Al}/\{1\,1\,1\}_{Al}$ interfacial energy anisotropy decreases gradually as the temperature increases above the melting point.

5. Liquid tin droplets embedded in an aluminium matrix solidify in three stages. Firstly, the larger tin

droplets at the aluminium grain boundaries solidify by nucleation on catalytic trace impurities, over a temperature range of approximately 170–140 °C. Secondly and thirdly, the smaller tin droplets embedded within the aluminium grains solidify by catalytic nucleation on the $\{1\,0\,0\}_{Al}$ $\{1\,1\,1\}_{Al}$ facets over the two temperature ranges of approximately 140–128 °C and 128–115 °C.

6. Catalytic nucleation of the solidification of tin takes place at special sites such as steps or dislocations on the $\{1\,0\,0\}_{Al}$ and $\{1\,1\,1\}_{Al}$ facets, with contact angles of 55° and 59°.

Acknowledgements

We thank Professor Sir Peter Hirsch for provision of laboratory facilities. One of us (WTK) would like to thank the Korea Science and Engineering Foundation for financial support.

References

1. J. W. CHRISTIAN, "The Theory of Transformations in Metals and Alloys" (Pergamon, Oxford 1975).
2. B. VONNEGUT, *J. Colloid Sci.* **3** (1948) 563.
3. D. TURNBULL, *J. Chem. Phys.* **18** (1950) 768.
4. J. H. PEREPEZKO, D. H. RASMUSSEN, I. E. ANDERSON and C. R. ROPER, "Solidification and Casting of Metals" (Metals Society, London, 1979) p. 169.
5. Y. MIYAZAWA and G. M. POUND, *J. Crystal Growth* **23** (1974) 45.
6. J. H. PEREPEZKO *et al.*, "Rapid Solidification Processing: Principles and Technology", edited by R. Mehrabian, B. H. Kear and M. Cohen (Claitors, Baton Rouge, 1980) p. 56.
7. J. H. PEREPEZKO, *Mater. Sci. Engng* **65** (1984) 125.
8. J. H. PEREPEZKO and J. S. SMITH, *J. Non-Cryst. Solids* **44** (1981) 65.
9. J. H. PEREPEZKO and J. S. PAIK, *ibid* 61/62 (1984) 113.
10. M. G. CHU, Y. SHIOHARA and M. C. FLEMINGS, *Met. Trans.* **15A** (1984) 1303.
11. D. TURNBULL and R. E. CECH, *J. Appl. Phys.* **21** (1950) 804.
12. D. TURNBULL, *J. Metals* **188** (1950) 1144.
13. M. J. STOWELL, *Phil. Mag.* **22** (1970) 1.
14. R. E. SUNDQUIST and L. F. MONDOLFO, *Trans. AIME* **221** (1961) 157.
15. R. E. CECH and D. TURNBULL, *ibid.* **206** (1956) 124.
16. A. J. DREHMAN and A. L. GREER, *Acta Metall.* **32** (1984) 323.
17. A. J. DREHMAN and D. TURNBULL, *Scripta Metall.* **15** (1981) 543.
18. G. H. ABBASCHIAN and M. C. FLEMINGS, *Met. Trans.* **14A** (1983) 1147.
19. T. Z. KATTAMIS and M. C. FLEMINGS, *Trans. TMS-AIME* **236** (1966) 1523.
20. W. T. KIM, PhD thesis, Seoul National University, Seoul (1987).
21. J. FEHLING and E. SCHEIL, *Z. Metallkde* **53** (1962) 593.
22. S. N. OJHA, T. R. ANANTHARAMAN and P. RAMACHANDRARAO, *J. Mater. Sci.* **17** (1982) 264.
23. T. Z. KATTAMIS and M. C. FLEMINGS, *Met. Trans.* **1** (1970) 1449.
24. K. I. MOORE, D. L. ZHANG and B. CANTOR, *Acta Metall.*, in press.
25. C. C. WANG and C. S. SMITH, *Trans. AIME* **188** (1950) 136.
26. R. T. SOUTHIN and G. A. CHADWICK, *Acta Metall.* **26** (1978) 223.
27. P. G. BOSWELL and G. A. CHADWICK, *ibid.* **28** (1980) 209.
28. K. I. MOORE, K. CHATTOPADHYAY and B. CANTOR, *Proc. Roy. Soc.* **A414** (1987) 499.
29. K. I. MOORE and B. CANTOR, in "Solidification and Casting of Metals II" (Metals Society, London, 1987) p. 515.
30. D. L. ZHANG and B. CANTOR, *J. Mater. Sci.*, in press.
31. *Idem, Phil. Mag.*, **A62** (1990) 557.
32. A. J. McALISTER and D. J. KAHAN, *Bull. Alloy Phase Diag.* **4** (1983) 410.
33. G. WULFF, *Z. Kristallogr.* **53** (1901) 440.
34. D. TURNBULL, *J. Appl. Phys.* **21** (1950) 1022.
35. B. CANTOR and R. D. DOHERTY, *Acta Metall.* **27** (1979) 33.
36. W. T. KIM, D. L. ZHANG and B. CANTOR, *Met. Trans.* in press.
37. L. M. MONDOLFO, N. L. PARISI and G. J. KARDYS, *Mat. Sci. Engng* **68** (1984–85) 249.
38. E. A. BRANDES and C. J. SMITHELLS, "Metals Reference Book", 6th Edn (Butterworths, London, 1983).

Received 12 January
and accepted 16 May 1990